A&A 570, A53 (2014)
DOI: 10.1051/0004-6361/201424332

Astronomy & Astrophysics

SALT long-slit spectroscopy of CTS C30.10: two-component Mg II line⋆,⋆⋆,⋆⋆⋆

J. Modzelewska[1], B. Czerny[1], K. Hryniewicz[1,3], M. Bilicki[2], M. Krupa[4], A. Świętoń[4], W. Pych[1], A. Udalski[5], T. P. Adhikari[1], and F. Petrogalli[1]

[1] Nicolaus Copernicus Astronomical Center, Bartycka 18, 00-716 Warsaw, Poland
e-mail: bcz@camk.edu.pl
[2] Astrophysics, Cosmology and Gravity Centre, Department of Astronomy, University of Cape Town, Rondebosch, South Africa
[3] ISDC Data Centre for Astrophysics, Observatoire de Genève, Université de Genève, Chemin d'Ecogia 16, 1290 Versoix, Switzerland
[4] Astronomical Observatory of the Jagiellonian University, Orla 171, 30-244 Cracow, Poland
[5] Warsaw University Observatory, Al. Ujazdowskie 4, 00-478 Warszawa, Poland

Received 3 June 2014 / Accepted 5 August 2014

ABSTRACT

Context. Quasars can be used as a complementary tool to SN Ia to probe the distribution of dark energy in the Universe by measuring the time delay of the emission line with respect to the continuum. The understanding of the Mg II emission line structure is important for cosmological application and for the black hole mass measurements of intermediate redshift quasars.
Aims. Knowing the shape of Mg II line and its variability allows for identifying which part of the line should be used to measure the time delay and the black hole mass. We thus aim at determining the structure and the variability of the Mg II line, as well as the underlying Fe II pseudo-continuum.
Methods. We performed five spectroscopic observations of a quasar CTS C30.10 (z = 0.9000) with the SALT telescope between December 2012 and March 2014, and we studied the variations in the spectral shape in the 2700 Å−2900 Å rest frame.
Results. We show that the Mg II line in this source consists of two kinematic components, which makes the source representative of type B quasars. Both components were modeled well with a Lorentzian shape, and they vary in a similar way. The Fe II contribution seems to be related only to the first (blue) Mg II component. Broad band spectral fitting instead favor the use of the whole line profile. The contribution of the narrow line region to Mg II is very low, below 2%. The Mg II variability is lower than the variability of the continuum, which is consistent with the simple reprocessing scenario. The variability level of CTS C30.10 and the measurement accuracy of the line and continuum is high enough to expect that further monitoring will allow the time delay between the Mg II line and continuum to be measured.

Key words. accretion, accretion disks – techniques: spectroscopic – line: profiles – quasars: individual: CTS C30.10 – dark energy – galaxies: active

1. Introduction

Quasars represent the high luminosity tail of active galactic nuclei (AGN). They are numerous and can be easily detected at cosmological distances, so they can be used to investigate the properties of the Universe. They are used to probe the intergalactic medium (e.g., Sargent 1977; Bordoloi et al. 2014), they provide information on the massive black hole growth (e.g., Kelly et al. 2010), and they have recently been proposed as promising tracers of the expansion of the Universe (Watson et al. 2011; Czerny et al. 2013; Marziani & Sulentic 2014a,b; Wang et al. 2013; Hoenig 2014; Yoshii et al. 2014). The last two aspects mostly rely on the presence of the broad emission lines in the quasar spectra. The broad line region (BLR) is not resolved but the shapes of the lines and, in particular, the variability of the lines and of the continuum are keys to understanding the quasar structure. This is interesting by itself and essential for the follow-up applications.

Systematic studies of the continuum and line variability have been done extensively for nearby AGN for many years (Clavel et al. 1991; Peterson 1993; Reichert et al. 1994; Wandel et al. 1999; Kaspi et al. 2000; Peterson et al. 2004; Metzroth et al. 2006; Bentz et al. 2013). Most studies were done for the Hβ line since this line is easily measured in the optical band for sources with redshift below ~0.3. The line belongs to the family of the low ionization lines (Collin-Souffrin et al. 1988), which do not show considerable shifts with respect to the host galaxy. Finally, the nearby narrow [OIII] forbidden line helps to calibrate the spectra. Mg II and CIV lines were followed when there was UV data available, but for high redshift quasars they are the only alternative for studies in the optical band. Mg II is suitable for sources with redshifts between 0.4 and 1.5, and CIV for quasars with redshift above 1.7. In the present paper we concentrate on the Mg II line.

The Hβ line was found to generally be a good indicator of the black hole mass, and the emitting material indeed seems roughly in Keplerian motion. Several authors (e.g., Kong et al. 2006; Shen et al. 2008; Vestergaard & Osmer 2009) have concluded

⋆ Based on observations made with the Southern African Large Telescope (SALT) under program 2012-2-POL-003 and 2013-1-POL-RSA-002 (PI: B. Czerny).
⋆⋆ Spectra shown in Figs. 3 and 4 are only available in electronic form at the CDS via anonymous ftp to cdsarc.u-strasbg.fr (130.79.128.5) or via http://cdsarc.u-strasbg.fr/viz-bin/qcat?J/A+A/570/A53
⋆⋆⋆ Table 1 is available in electronic form at http://www.aanda.org

that Mg II also gives quite satisfactory results for the black hole mass measurement. The Vanden Berk et al. (2001) composite quasar spectrum from SDSS also indicated no shifts of Mg II with respect to the expected position. However, with the increased need for accuracy, several problems started to appear. Wang et al. (2009) showed that the full width at the half maximum (FWHM) of Mg II in many sources is lower by ∼20 % than FWHM of Hβ. Relations between the two lines can thus be found but with considerable scatter (Shen & Liu 2012; Trakhtenbrot & Netzer 2012). Marziani et al. (2013a,b) analyzed 680 quasars from the Sloan Digital Sly Survey (SDSS) with both lines visible in their spectra and concluded that, overall, Mg II is a good black hole mass indicator if carefully used. They analyzed the results following the quasar division of Sulentic et al. (2007) into two classes. For type A sources, with FWHM of Hβ below 4000 km s^{-1}, the Mg II line is simply narrower than Hβ by 20%. The line is well fit by a single Lorentzian. We found the same single Lorentzian shape in the excellent SALT spectrum of LBQS 2113-4538, which also belongs to this class. However, for type B sources (with FWHM of Hβ above 4000 km s^{-1}) the Mg II line consists of two components, with a nearly unshifted broad component and a redshifted very broad component (Marziani et al. 2009, 2013b). Marziani et al. (2013b) suggest that only the broad component should be used for determining the black hole mass.

The results of Marziani et al. (2013a,b) were based on an analysis of the composite spectra since a single SDSS spectrum has too low a signal-to-noise ratio to perform a multicomponent fit reliably. With SALT data, we can do this decomposition for bright sources. The object CTS C30.10 discussed in this paper is of type B class and requires such a complex approach.

2. Observations

CTS C30.10 is one of the quasars found in the Calan-Tololo Survey, which aims to identify new bright quasars in the southern part of the sky. The source is located at RA = 04h47m19.9s, Dec = −45d37m38s. The quasar nature of the source was confirmed using the slit spectroscopy (Maza et al. 1993). The source is relatively bright for an intermediate redshift quasar ($z = 0.910$, $V = 17.2$, as given in NED[1]), so we selected it for a detailed study of the Mg II line, together with LBQS 2113-4538 (Hryniewicz et al. 2014).

2.1. Spectroscopy

We observed the quasar CTS C30.10 with the use of the Robert Stobie Spectrograph (RSS; Burgh et al. 2003, Kobulnicky et al. 2003; Smith et al. 2006) on the Southern African Large Telescope (SALT) in service mode. The observations were made on the nights of Dec 6/7 in 2012, of January 21/22, March 20/21, and August 4/5 2013, and of March 5/6 in 2014. Every observation consisted of two 739 second exposures in a long-slit mode, with the slit width of 2″, an exposure of the calibration lamp, and several flat-field images. As for LBQS 2113-4538, we used RSS PG1300 grating, corresponding to the spectral resolution of $R = 1047$ at 5500 Å. We used the blue PC04600 filter for the order blocking.

The nights were photometric, without intervening clouds. Observations 1, 2, 3, and 5 were performed in gray moon conditions, and Observation 4 in dark moon conditions. The seeing was good in Observation 4 (∼1.4″) and somewhat worse in the previous three data sets (∼1.5″−2.4″), as well as in the last observation (∼1.9″).

The basic data reduction was done by SALT staff using a semi-automated pipeline from the SALT PyRAF package[2] (see Crawford et al. 2010). Further steps, including flat-field correction, were done by us with the help of IRAF package[3]. Two consecutive exposures were combined to increase the signal-to-noise ratio and to remove the cosmic ray effects. After proper wavelength calibration, we extracted one-dimensional spectra using the noao.twodspec package within IRAF.

Since the SALT telescope has several problems with vignetting that affects the broad band spectral shape, we used SALT observations of the spectroscopic standards. A number of stars with well-calibrated spectra available at ESO were observed by SALT with a similar telescope setup to the one used in our quasar observations. We finally selected the star LTT1020, which was observed with SALT on Oct. 3, 2012, with the instrumental setup PG1300/23.375 (spectrum P201210130322). This is a relatively bright G-type star ($V = 11.52$) that does not show any significant absorption lines in the 5000−5600 Å band. The ESO spectrum for this star was downloaded from the ESO website[4]. We obtained the ratio of the star spectrum from SALT to the calibrated star spectrum from ESO in the 5000−5700 Å wavelength range. In next step we normalized this ratio to 1 in the middle of the interesting wavelength range, and we fit this ratio with a quadratic function. The derived analytical formula was treated as a telescope response for the five SALT spectra of quasar CTS C30.10. The same correction was used for all spectra. The method allowed us to obtain the correct shape of the spectra but not the absolute calibration. However, this already allows for determining the emission lines in the individual spectra. At that stage the spectra were ready for further analysis. We neglected the instrumental broadening since we have shown before (Hryniewicz et al. 2014) that it is unimportant for SALT quasar emission lines.

The effect of the Galactic extinction was removed, although the extinction in the direction of CTS C30.10 is very low (A_λ = 0.038, 0.029, and 0.023 in the B,V and R bands; Schlafly & Finkbeiner 2011 after NED). We neglected the intrinsic absorption as there is no clear signature of such an extinction in the spectra. We also neglected a possible host galaxy contribution as it is not likely to be important at such short wavelengths.

2.2. Photometry

The spectroscopic observations of CTS C30.10 were supplemented with the photometric data. Photometry was collected as a subproject of the OGLE-IV survey with the 1.3-m Warsaw Telescope and 32 CCD mosaic camera, located at the Las Campanas Observatory, Chile. CTS C30.10 was monitored approximately every two weeks between September 2012 and March 2014 in the V-band with the exposure time set to 240 s. Collected images were reduced using the standard OGLE photometry pipeline (Udalski 2003). The accuracy of a single measurement of CTS C30.10 was better than 0.01 mag. OGLE observations reveal long-term photometric changes of CTS C30.10

[1] NASA/IPAC Extragalactic Database (NED) is operated by the Jet Propulsion Laboratory, California Institute of Technology.

[2] http://pysalt.salt.ac.za

[3] IRAF is distributed by the National Optical Astronomy Observatories, which are operated by the Association of Universities for Research in Astronomy, Inc., under cooperative agreement with the NSF.

[4] ftp://ftp.eso.org/pub/stecf/standards/ctiostan/

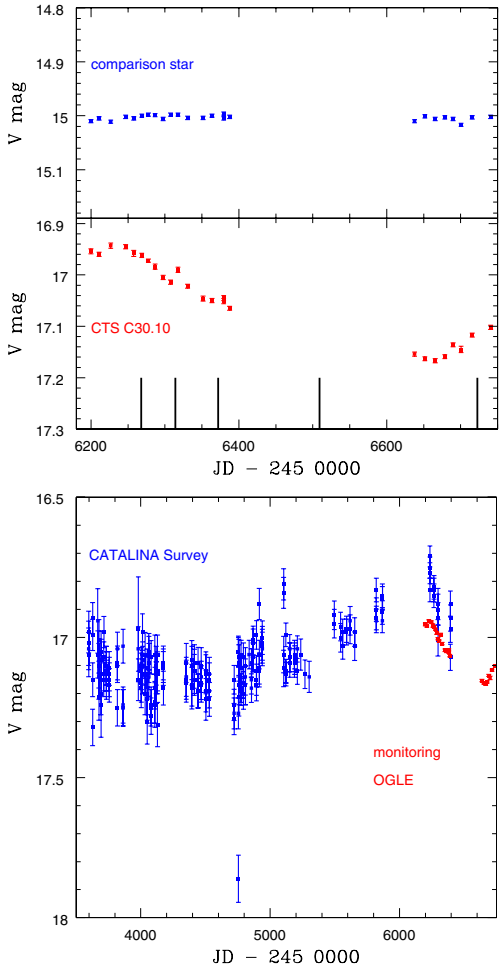

Fig. 1. V-band light curve of CTS C30.10 (*middle panel*) and one for the comparison star (*upper panel*) from OGLE monitoring, with times of spectroscopic measurements shown by vertical lines. The *lower panel* shows the Catalina lightcurve, together with the OGLE lightcurve.

on the time scale of about a year. The stability of the zero point of the photometry was verified by checking several nearby constant stars. OGLE light curve of CTS C30.10 is presented in Fig. 1 (two upper panels).

We supplemented these short data set with much longer, but less accurate photometry from Catalina survey (Catalina RTS; Drake et al. 2009) which covers the past eight years. The observed trends are shown in the lower panel of Fig. 1. Overall, the CATALINA lightcurve is consistent with high quality OGLE data. There is one strange outlier well below the other data points. If real, it would imply a flux change by a factor 2 in 16 seconds, which we consider unlikely. The CATALINA position of the source in this particular measurement is strangely shifted by 0.5″, so probably the source was at the edge of the field of view of the instrument.

2.3. Broad band spectrum

For the purpose of insight into the broad band spectral shape, we also collected the data through the ASDC Sky Explorer/SED Builder web interface[5] and GALEX View[6]. Photometric points come from the following data products: WISE (Wright et al. 2010), 2MASS (Skrutskie et al. 2006), USNO A2.0, USNO B1,

[5] http://tools.asdc.asi.it/
[6] http://galex.stsci.edu/GalexView/

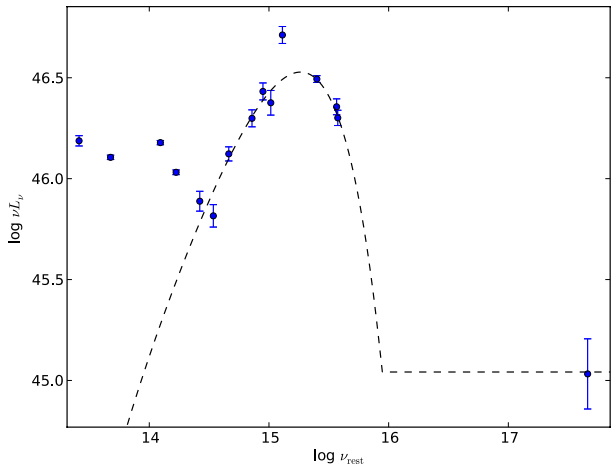

Fig. 2. Time-averaged broad band spectrum of CTS C30.10, together with the parametric fit based on Eq. (1). The IR contribution comes from the circumnuclear dust and the host galaxy.

GALEX (Martin et al. 2005), and RASS (Voges et al. 1999). The data points were dereddened assuming $E(B-V) = 0.009$ from NED and applying the extinction curve of Cardelli et al. (1989) for a standard value of $R_V = 3.1$. Those points are multi-epoch data.

The broad band spectrum is shown in Fig. 2. This spectrum is based on observations derived in the time span of several years so it is not surprising that some points depart from the overall shape. If more data points were available at a given wavelength, like in the V band, we averaged them to show the CTS C30.10 spectral energy density (SED) more clearly. The optical/UV/X-ray part of the spectrum is represented well by a simple approximation to a disk-plus-X-ray power-law shape in the form of

$$F_\nu = A\nu^{\alpha_{uv}} \exp(-h\nu/kT_{\rm BB}) \exp(-kT_{\rm IR}/h\nu) + B(\alpha_{\rm ox})\,\nu^{\alpha_x} \qquad (1)$$

with the following values of the parameters: $T_{\rm BB} = 4.8 \times 10^4$ K, $\alpha_{uv} = 0.95$, $\alpha_x = -1$, and $\alpha_{\rm ox} = -1.55$. The choice of $\alpha_x = -1$ was arbitrary but consistent with the broad band composite shape (Laor et al. 1997a; Elvis et al. 2012). With appropriate proportionality constants A and B, this fit is shown in Fig. 2 by a dashed line. It represents the contribution of an accretion disk and X-ray compact source to the total spectrum. The value of $T_{\rm BB}$ is moderate and hints at a moderate Eddington ratio in the quasar. The point based on the USNO catalog (B band) is much above the expected trend. This catalog is based on very old Palomar Observatory Sky Survey plates. Therefore, two effects could be responsible for the shift: either the measurement accuracy is worse than the provided errorbar, or quasar variability over the years could account for that. We do not have the precise date for that observation, but the measurement is much older than most of the other SED points.

3. Model

We aim to model the spectrum in the relatively narrow band, between the 2700 Å and 2900 Å rest frames, so we assume that the spectrum consists of three components: power-law continuum, Fe II pseudo-continuum, and Mg II line. The line apparently has a much more complex shape than the single-Lorentzian shape found for LBQS 2113–4538, so we allow for two separate kinematic components in the line itself, represented either as

Lorentzians or as Gaussians. As an alternative, we also consider a single component in emission and a second component in absorption. Each of the kinematic components is modeled either as a single line emitted at 2800 Å or as a doublet (2796.35, 2803.53; Morton 1991). The doublet ratio is usually fixed at 1:1, but we check as well the sensitivity of the solution to this assumption and search for the best-fit ratio. We also vary the redshift of the object since the previously collected data used for redshift determination did not have high quality (Maza et al. 1993).

The Fe II UV pseudo-continuum is modeled by a choice of theoretical and observational templates. We tested the classical observational template of Vestergaard & Wilkes (2001) and Tsuzuki et al. (2006) based on I Zw 1. Theoretical templates were taken from Bruhweiler & Verner (2008), with each of them calculated for different values of the density, turbulent velocity, and ionization parameter Φ. Finally, we used the observational template derived by Hryniewicz et al. (2014) as a byproduct of the analysis of the LBQS 2113-4538. We allowed for Fe II broadening, as well as for the shift with respect to Mg II, since it was suggested that Fe II comes from infalling material (Ferland et al. 2009).

4. Results

We analyzed five spectra of the quasar CTS C30.10 obtained with the SALT telescope between December 2012 and March 2014. Spectra were analyzed separately since the photometric lightcurve shows a systematic decrease in the source luminosity between December 2012 and January 2014, later replaced by a brightening trend so we searched for the corresponding variability in the spectral shape. Using the photometry, we also attempted to calibrate the spectra properly and to obtain the rms spectrum for our source. We modeled the relatively narrow spectral range in detail, 2700−2900 Å in the rest frame of the object, since broader band data from SALT cannot be calibrated in a reliable way. Narrow band spectral fitting, however, is enough to give insight into the structure of the Mg II line and its time variability.

4.1. Separate spectra

All spectra have high signal-to-noise ratios, in the range of 30 to 50, with the 579 pixels covering the 2700−2900 Å rest frame band. All five spectra are clearly asymmetric in the Mg II region. This is frequently seen in the quasar Mg II line shape spectra (e.g., Vestergaard & Wilkes 2001; Dietrich et al. 2002; Woo 2008), and may be interpreted as the multicomponent nature of emission. In particular, two-component fits to Mg II line were used by Dietrich et al. (2003), and the distinction between the broad line region and the very broad line region is made as the basis of such an analysis. In their analysis of the quasar properties from SDSS DR7, Shen et al. (2011) used a single Gaussian to represent the contribution from the narrow line region (NLR), and one to three Gaussians to describe the broad line, while Hu et al. (2008) and Wang et al. (2009) used five-parameter Gauss-Hermite series for the broad component. We first followed this general interpretation and study pure emission model of the chosen spectral region. However, we fit the continuum, Fe II pseudo-continuum, and the Mg II line at the same time.

The contribution from the Fe II pseudo-continuum may in principle be responsible for the apparent Mg II asymmetry. This was the case for the previously studied quasar LBQS 2112-4538 (Hryniewicz et al. 2014), which belongs to type A sources. To check whether CTS C30.10 can also be modeled with only a single component, we used several Fe II templates, but for all of them the Mg II was much better represented when two kinematic components were used for the line, and the difference in χ^2 between single kinematic component and two kinematic components was very large. We give just one example of a single component fit for each observation in Table 1 to illustrate this effect. The doublet nature of the two components is not directly visible in the spectra so we used the solutions with a doublet ratio 1:1 as a default. Any change in that ratio does not improve a single-component fit considerably.

We thus consider two-component fits for Mg II, with both components in emission or one in emission, and one in absorption. In both cases, we again use a 1:1 doublet description of each of the kinematic components as a default.

4.1.1. Two Mg II components in emission

We consider two kinematic components for the emission of Mg II, described either as Gaussians or Lorentzians. However, we described the underlying Fe II emission as a single kinematic component. Fe II component was assumed to have the same redshift as the first (blue) Mg II component, and the best fits in almost all cases were obtained for redshift 0.9000, with an accuracy of the redshift measurement of 0.0004. This redshift, centered on the first component, is clearly lower than $z = 0.910$ as determined by Maza et al. (1993). The shift of the second component was a free parameter of the model.

The best fits were always obtained for a two-Lorentzian model of the Mg II shape. Fits based on two Gaussians have χ^2 much higher than two Lorentzian fits, as we illustrate in Table 1 for a few cases. We thus further constrain our discussion to the two Lorentzian case. The fits depend to some extent on the choice of the Fe II template. In each observation another template gives the best fit. However, for each observation a number of templates give acceptable results within a one-sigma error. The values of the EW for Mg II and Fe II are also partly dependent on the template, although not much for the templates that give the lowest χ^2 values.

To study the time dependence of the parameters, it is better to select a fixed Fe II template. The template 13 (theoretical template d12-m20-20-5 of Bruhweiler & Verner 2008), with the Gaussian broadening, for a half width of 900 km s^{-1} is always in the group of acceptable templates for all five observations, so we consider this template as the best. We thus show fits for this choice of the Fe II for all five observations in Table 2, including the parameter errors. These fits to the five spectra are shown in Fig. 3.

The source shows significant evolution. The total equivalent width (EW) of Mg II line increases monotonically with time as the continuum gets fainter. Both kinematic components show a significant increase. The ratio between the two components, however, does not show any clear trend. It varies from 0.37 to 0.58 in various data sets, but the error of the component ratio is greater than the error of the total line EW, on the order of 0.08, and such variations are in fact consistent with a constant fraction within a two-sigma error. The line width of the first component is constant within the measurement accuracy. The second component seems to vary more: it is significantly narrower (~2600 instead of ~3500 km s^{-1}) in Observation 3 and somewhat lower in Observation 5 than in the other three data sets. This behavior is not accompanied by any other considerable change in the fit parameters. However, the error of the FWHM of

Table 2. Summary table of the fits of Mg II with errors for the template 13 and two Lorentzian components in emission for five individual spectra obtained with SALT between December 2012 and March 2014.

Obs.	Mg II *EW* total Å	Mg II *L* total 10^{-14}erg s^{-1} cm^{-2}	Mg II *FWHM* comp. 1 km s^{-1}	Mg II *EW* comp. 1 Å	Mg II *FWHM* comp. 2 km s^{-1}	Mg II *EW* comp. 2 Å	Fe II *EW* Å	Fe II *L* 10^{-14}erg s^{-1} cm^{-2}
1	$25.63^{+0.22}_{-0.13}$	$2.95^{0.06}_{-0.05}$	2871^{+170}_{-110}	$17.1^{+1.0}_{-0.8}$	3470^{+380}_{-330}	$8.5^{+0.9}_{-0.7}$	$6.98^{+0.71}_{-2.07}$	$0.80^{+0.08}_{-0.23}$
2	$26.51^{+0.24}_{-0.14}$	$2.89^{0.06}_{-0.05}$	2850^{+210}_{-140}	$16.9^{+1.3}_{-1.0}$	3438^{+510}_{-400}	$9.6^{+1.2}_{-0.9}$	$8.38^{+1.03}_{-3.41}$	$0.91^{+0.11}_{-0.37}$
3	$27.45^{+0.45}_{-0.07}$	$2.93^{0.08}_{-0.05}$	2750^{+350}_{-40}	$19.7^{+1.8}_{-1.0}$	2636^{+600}_{-400}	$7.8^{+1.5}_{-1.0}$	$10.21^{+2.05}_{-2.03}$	$1.08^{+0.23}_{-0.23}$
4	$29.47^{+0.22}_{-0.09}$	$2.94^{0.06}_{-0.05}$	2850^{+140}_{-140}	$18.3^{+1.0}_{-0.8}$	3666^{+390}_{-320}	$11.2^{+1.0}_{-0.7}$	$11.30^{+1.89}_{-0.86}$	$1.12^{+0.20}_{-0.09}$
5	$29.82^{+0.33}_{-0.60}$	$2.76^{0.06}_{-0.08}$	2728^{+170}_{-120}	$19.3^{+1.0}_{-1.0}$	3338^{+550}_{-410}	$10.5^{+0.8}_{-0.8}$	$11.21^{+0.98}_{-2.31}$	$1.03^{+0.09}_{-0.21}$

Table 3. Spectral fits for the template 13 of Fe II, a Lorentzian component in emission, and a Gaussian component in absorption, for five individual spectra obtained with SALT between December 2012 and March 2014.

Obs.	Slope	Mg II *EW* emission Å	Mg II *FWHM* emission km s^{-1}	Mg II *EW* absorption Å	Mg II *FWHM* absorption km s^{-1}	Fe II *EW* Å	χ^2
1	–1.501	36.62	3109	–16.18	1618	1.57	269.3
2	–1.458	35.60	3175	–14.18	1577	1.63	401.3
3	–1.587	38.81	3000	–16.49	1452	3.49	207.6
4	–1.893	36.70	3809	–9.62	1455	3.78	722.6
5	–2.021	41.38	3072	–17.61	1561	3.71	300.9

the second component is also larger so the change cannot be considered as significant. The relative shift between the two components did not vary: for all five observations the shift was consistent with the mean value of 2780 km s^{-1} within a one-sigma error. The Fe II EW given in Tables 1 and 2 is measured between 2700 and 2900 Å rest frame. This value is rising with the Mg II line.

Since the continuum decreases, as seen in Fig. 1, we checked whether this change simply reflects the change in the continuum or if it reflects the intrinsic change in the Mg II and Fe II luminosity. The errors are large, but the change in Mg II is nevertheless significant (see Table 2). The luminosity is consistent with being constant for the first four observations, followed by a decrease in Observation 5. The decrease is not large, only 6%, but it is highly significant. The Fe II luminosity seems to be rising, followed by a decrease in Observation 5, but errors are large. The change in the line intensity is four times less than the change in the continuum (23%, as seen in OGLE monitoring). Thus the variability we see in Mg II is less than observed by Woo (2008) but consistent with the average Mg II efficiency of $\eta \sim 0.2$ (Goad et al. 1999; Korista & Goad 2004; Kokubo et al. 2014).

Results given in Table 2 were obtained for a fixed 1:1 ratio for the Mg II doublet. We tested this assumption for Observation 5. The best fit value was obtained for the 1.6:1 ratio and the redshift 0.90052, but all values of the doublet ratio are acceptable within a two-sigma error. The EW(Mg II) line depend only weakly on the value of that ratio and changed from 29.82 Å for a 1:1 ratio to 29.90 Å for 1.6:1.

Fits given in Table 1 are based on the assumption that there is no net shift in the Fe II with respect to the blue component of Mg II. We tested this assumption in detail for Model M of Observation 5. If the relative velocity of Fe II and Mg II is treated as another free parameter of the model, the minimum is reached for the value of 450 km s^{-1}. (The χ^2 dropped by 6.8, and all values between 180 km s^{-1} and 820 km s^{-1} are acceptable within a one-sigma error.) Introduction of this relative velocity between the Fe II and Mg II did not change the EW(Mg II) significantly, therefore we did not repeat all the fitting with this new parameter included, since this would mean introducing still one more free parameter.

Since there are two Mg II components, we also checked whether two components are needed to describe Fe II contribution. Since we did not want to introduce too many additional free parameters, we assumed that the second Fe II kinematic component is in the same proportion to the first one as the two Mg II components, and we assumed the same velocity shift for the second (red) component of Fe II. The fit was slightly worse (the χ^2 was higher by 21), so the second Fe II component was clearly ruled out. This can be understood simply by looking at the shape of the spectrum: there is a clear trace of the Fe II peak at ~2750 Å in the observed spectrum, as well as in the templates, and a composition of two shifted templates smears this feature too much in the model.

4.1.2. Contribution from the narrow line region

In the fits above we neglected any possible contribution from the NLR to the Mg II line. The spectra do not seem to show a narrow top but in principle, the NLR contribution can still be hidden in the Mg II complex profile due to the relatively low spectral resolution. Therefore, we considered fits with the NLR contribution on the top of the two-component broad Mg II line. We fixed the FWHM of the narrow line at 600 km s^{-1} and modeled the line as a single Gaussian in an arbitrary position. However, the χ^2 always dropped. Any contribution from the NLR at a level higher than 2% is ruled out. Therefore, CTS C30.10 in this respect is similar to the type A source LBQS 2113-4538, where the separate NLR contribution to Mg II was also not detected (Hryniewicz et al. 2014).

4.1.3. Emission/absorption interpretation

Since we do not see any significant difference in the time behavior of the two emission components, we considered an

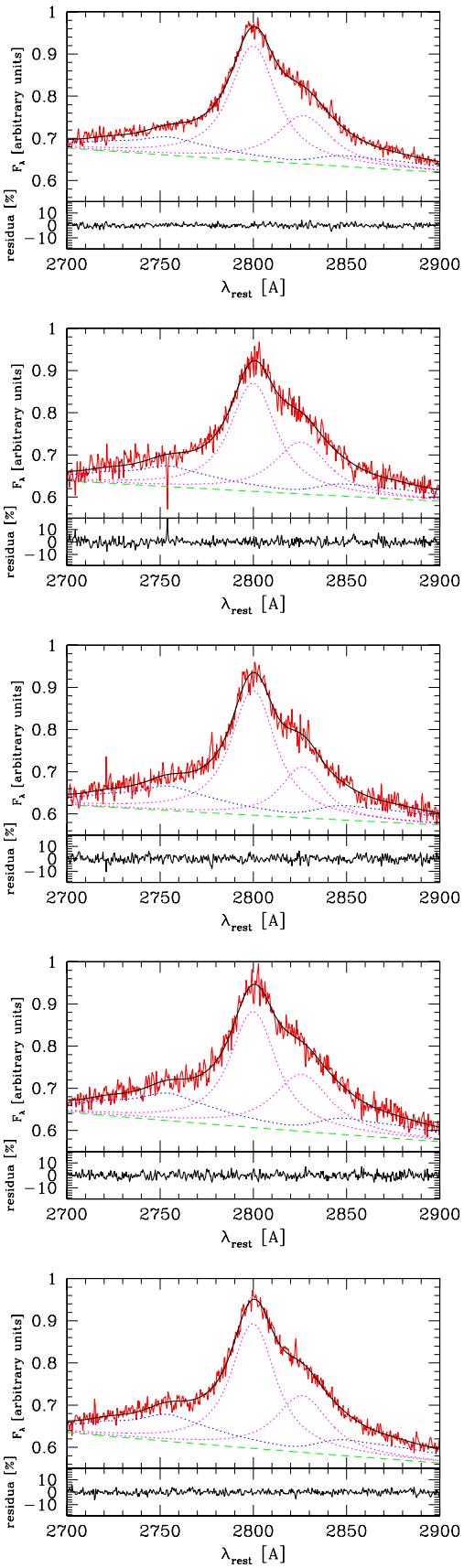

Fig. 3. Best fit and residuals for five observations, model M (see Table 1 for model parameters); continuous lines show the model and the data, dashed lines give the underlying power law, the dotted blue line represents the kinematically blurred Fe II pseudo-continuum, and dotted magenta lines mark the two kinematic components of the Mg II.

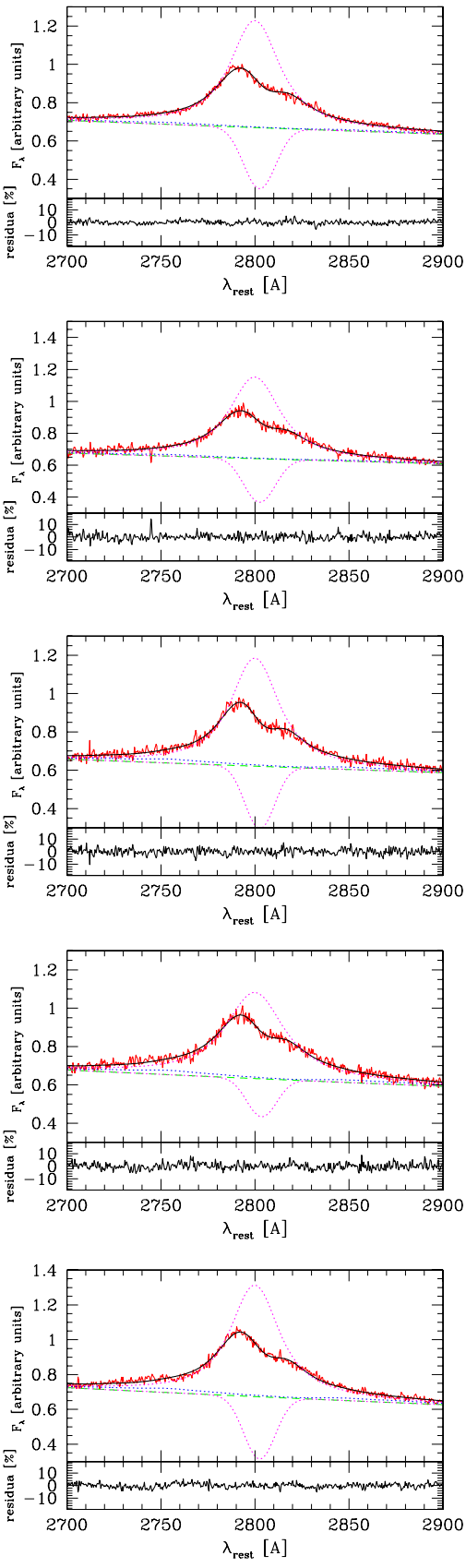

Fig. 4. Best fit and residuals for five observations, model M (see Table 3 for model parameters); continuous lines show the model and the data, dashed lines give the underlying power law, the dotted blue line represents the kinematically blurred Fe II pseudo-continuum, and dotted magenta lines mark the emission and absorption components of the Mg II.

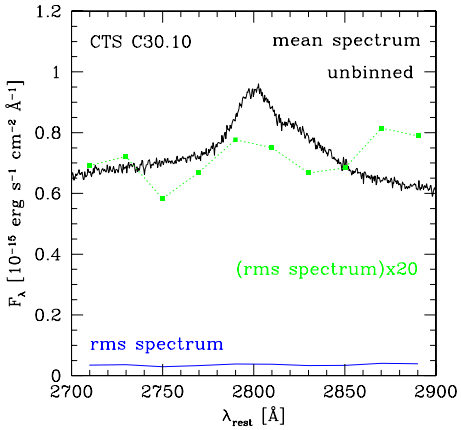

Fig. 5. Mean (black line) and binned (blue line) rms spectrum of CTS C30.10. We also plot the rms value multiplied arbitrarily by a factor of 20 (green line) for better visibility.

alternative model with a single broad component in emission and a narrower component in absorption. Such a model would immediately explain why the two wings, or emission components, vary together. We explored this interpretation in detail only for Fe template 13. We modeled emission as a single Lorentzian and absorption as a single Gaussian. Such a model has exactly the same number of parameters as the previous model with two emission components. The resulting best fits for all five observations are shown in Fig. 4. For Observation 2 the fit with absorption is better than for both components in emission. For Observation 1 the two models are equally good and for Observations 3, 4, and 5 the pure emission model is better by 7, above 100 and 73 in χ^2. Thus, statistically, the absorption model is not favored. The errors of the fitted parameters are large since the absorption and emission have to compensate at ∼2800 Å.

4.2. Rms spectra

It is frequently advocated (e.g., Peterson et al. 2004) that rms spectra are better for the black hole mass determination. The shape of the rms spectrum may also indicate whether the two-component emission model is more justified, since in that case the variability of the two components may be different. We thus attempted to obtain such a spectrum for CTS C30.10 on the basis of four SALT spectra. The spectra, when corrected with the use of the spectroscopic standard, are not yet normalized properly. To obtain the correct normalization we use the photometric results. Three of the spectroscopic observations overlap with the OGLE photometry, and Observation 3 is in the gap. However, during this period the source seems to be systematically lowering its luminosity so we used the interpolation between the available photometric points. After this renormalization, we can obtain the rms spectra with the usual definition (see, e.g., Peterson et al. 2004)

$$F_{rms}(\lambda) = \left[\frac{1}{(N-1)}\sum_{i=1}^{N}(F_i(\lambda) - \overline{F(\lambda)})^2\right]^{1/2}, \quad (2)$$

where $\overline{F(\lambda)}$ is the average value obtained from a set of N spectra.

The resulting spectrum is shown in Fig. 5. The quality of the rms spectrum is very low since quasars vary slowly, and much longer time separations are needed to measure the spectrum variations more accurately. We had to bin the spectra considerably in order to get any signal. The variability seems lower in the regions contaminated more strongly by Fe II, while there is no clear difference in variability between the two kinematic components of the Mg II line. We tried to compare the variability of the two components by using bin size covering the two components in an optimum way (2770−2815 Å and 2815−2860 Å), but the ratio of the F_{var}/F_{mean} in such bins was quite similar, 0.037 ± 0.002 and 0.036 ± 0.002.

4.3. Global parameters

The Mg II line in CST C30.10 shows two kinematic components, and it is immediately not obvious how to apply the usual methods of the black hole mass determination. We therefore considered four possibilities: (i) to use Component 1; (ii) to use Component 2; (iii) to use a single-component fit to the spectrum; and (iv) to use the emission line parameters from the emission/absorption model, although the fit quality is much worse in the last two cases. We used three formulae for the black hole mass determination. The first one comes from Kong et al. (2006), their Eq. (7), the second one comes from Wang et al. (2009), their Eq. (10), and the third one from Trakhtenbrot & Netzer (2012). This last paper is particularly relevant since it contains the correction for the doublet character of Mg II, which is important for lines with the FWHM below 4000 km s^{-1} and is included in our analysis. The formulae are based on the knowledge of the monochromatic luminosity at 3000 Å and the FWHM of Mg II line, but differ slightly in the values of the coefficients. The monochromatic flux at 3000 Å was obtained from the photometric flux in V band (i.e., 2840 Å rest frame) using the standard cosmology (H_o = 71 km s^{-1} Mpc^{-1}, Ω_m = 0.270, Ω_Λ = 0.730). It was then extrapolated to the 3000 Å using the fitted spectral slope.

We also calculated the corresponding Eddington ratios. Bolometric luminosity was obtained from the monochromatic flux at 3000 Å by applying the bolometric correction from Richards et al. (2006), $L_{bol} = 5.62 \times \lambda L_\lambda(3000\ \text{Å})$.

The results obtained for Observation 2 are given in Table 4. The values based on Component 1 indicate a rather high Eddington ratio for all the formulae. This is not much expected since the sources with two-component and generally broader lines are believed to belong to the population B sources with lower Eddington ratios (Marziani et al. 2013a,b). The Eddington ratio for the type A quasar LBQS 2113-4538 studied before was 0.7 on the basis of the same Trakhtenbrot & Netzer (2012) formulae. If the classification into A and B sources is only applied to Component 1, the source should belong to class A. On the other hand, Marziani et al. (2013b) notice that some quasars do not quite follow the classification, and the BC class is actually a combination of type A2 and type B1 sources. The results based on the absorption model also give a fairly high Eddington ratio. Although the red and blue wings in this case are fitted with a single component, the line maximum is much higher than the one observed (peak is hidden by absorption). Component 2 gives a lower Eddington ratio, but that this component is not accompanied by the usual Fe II suggests a rather different origin than from the clouds close to the disk and in Keplerian motion.

A single-component fit implies a moderate Eddington ratio, and in low quality data such a solution would be satisfactory. However, we cannot neglect that a single component fit does not represent the data well. Results based on other observations are fairly similar, since neither the monochromatic luminosity nor the line kinematic width vary significantly.

We checked whether part of the problem lies in partial contamination of the V band by the Mg II and Fe II emission.

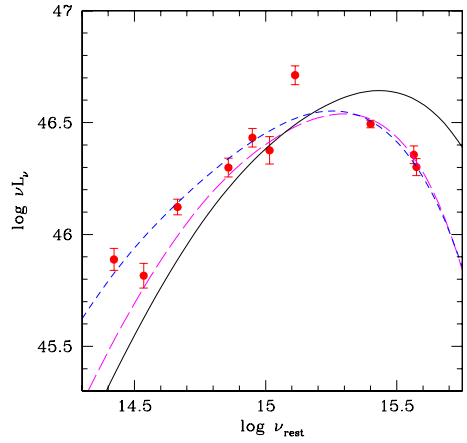

Fig. 6. Fits of Novikov-Thorne model to CTS C30.10 in the optical/UV band: (i) the black hole mass and Eddington ratio taken from Table 4, Component 1 only, Trakhtenbrot & Netzer formula (continuous line; Schwarzschild solution, best fit inclination of 63 deg); (ii) the same black hole mass but accretion rate arbitrarily fixed $L/L_{\rm Edd} = 0.35$ (long dashed line; best fit inclination – top view); (iii) single component fit (short dashed line; black hole spin $a = 0.9$, best fit inclination of 41 deg).

For that purpose, we calculated the fraction of the Mg II and Fe II emission in the V filter, taking the standard V filter profile and the spectral decomposition into account for Model M of Observation 2. The contamination is not strong as Mg II contributes 5.4%, and Fe II only 2.9%. This does not change the obtained Eddington ratio considerably, reducing it from 0.77 down to 0.71, for the Trakhtenbrot & Netzer (2012) formulae.

As an independent check of the appropriate values of the black hole mass and accretion rate in our object, we performed simple fits of an accretion disk to the broad band spectrum of CTS C30.10. We tested the black hole mass values based on the Mg II width and checked an applicable parameter range. As a disk model, we applied the simplest Novikov-Thorne model, with relativistic effects inluded, but without any color corrections or limb darkening effects to the local spectra.

The values of the black hole mass and the Eddington ratio derived from Component 1 and Trakhtenbrot & Netzer (2012) formulae, even for the Schwarschild black hole, overpredict the observed points above 3000 Å (see Fig. 6). Any positive black hole spin would make the fit only worse, but strong counter-rotation somewhat eases the problem. In addition, the implied inclination angle is quite large; otherwise, the discrepancy above 3000 Å is even stronger. If we use the black hole mass and the Eddington ratio from a single component fit, the predicted maximum temperature in the disk drops significantly, and the Schwarschild model represents the overall spectrum reasonably well. The required inclination angle is again rather large (60 deg) for a type 1 object. However, if we take the black hole mass derived from Component 1 and simply assume the Eddington ratio to be much lower than implied by the standard formula, we decrease the inclination angle easily. For the top view the implied Eddington ratio, 0.35, is relatively low and more consistent with the object line properties. Higher values of the black hole spin require adopting higher value for the black hole mass than given by Component 1. For example, a black hole spin of 0.9 and a black hole mass from a single component fit ($4.9 \times 10^9\ M_\odot$) give a very nice fit for an accretion rate of 0.055 and inclination angle of 41 deg. Formally, the last solution shows lower χ^2 than solutions for a Schwarzschild black hole, but we do not think that the quality of the available broad band spectrum is good enough to rely on the conclusions based on the curvature of the high frequency part of the spectrum which differentiates between the various spin models as a result of the relativistic effects. However, the low value of the accretion rate is another argument in favor of this class of solutions.

4.4. Covering factor

To have additional possible insight into the geometry of the emitting region, we estimated the covering factor required to produce the observed Mg II line EW. We used the observed continuum, but to have a rather smooth input continuum, we shifted down the B-band outlying point from USNO by 0.22 dex down in order to have a more realistic SED. This accounts for the Fe II contamination (7%) and variability amplitude seen in the CATALINA data. Calculations were performed with version 13.02 of Cloudy (Ferland et al. 2013). We adopted a single cloud approach since we do not have any other emission lines. We assumed the hydrogen column of 10^{23} cm^{-2} and a range of local densities between 10^{12} cm^{-3} and 10^{14} cm^{-3}, as is appropriate for a low ionization line (LIL) part of the BLR and consistent with the local densities at the accretion disk surface at the BLR distances (e.g., Rozanska et al. 2014). The results are not unique, mostly because of the uncertainty of the continuum in the E-UV and soft X-ray band. If we assume the broad band continuum as displayed in Fig. 2, we obtain the covering fraction in the range of 0.51−0.83. It is very high, but the covering factor is an old problem of the BLR, and various ways have been postulated to solve it (see, e.g., MacAlpine et al. 2003). However, if we assume that the source has significant soft X-ray excess, and instead of using a photon index $\Gamma = 2.0$ in the X-ray band, we simply interpolate between the last UV point and X-ray point (this gives $\Gamma = 2.65$), the covering factor reduces to 0.24−0.39.

4.5. Prospects for time delay measurement

Our measurements of the line intensity cover 15 months, and the same period is covered by the OGLE precise photometry. Earlier photometric monitoring is available from the CATALINA survey. We show these data in Fig. 1. Mg II line intensity is based on the two emission components of Mg II (see Sect. 4.1.1). Both photometry data sets confirm the presence of clear long-lasting trends in continuum, which should allow for the time delay measurement between the line and continuum. The line intensity does not vary significantly during the first four observations, but we see a drop in Observation 5, which may indicate that the line does respond to the change in the continuum. In addition, the CATALINA photometry is of too low a quality to attempt any delay measurement at this point. So far, the distant quasar monitoring has brought only the tentative measurement of a single object by Kaspi et al. (2007).

We can use the source redshift and the extinction-corrected interpolated monochromatic luminosity of 1.44×10^{46} erg s^{-1} at 5100 Å in the rest frame to estimate the expected time delay between the line and continuum. Using either the observational relation between the delay and flux from Bentz et al. (2013),

$$\log R_{\rm BLR} = 1.555 + 0.542 \log \frac{\lambda L_\lambda^{5100\text{Å}}}{10^{44}\text{erg s}^{-1}}\ [\text{lt. days}], \quad (3)$$

as obtained for nearby objects or by applying the dust-origin formula to the BLR size

$$\log R_{\rm BLR} = 1.244 + 0.5 \log \frac{\lambda L_\lambda^{5100\ \text{Å}}}{10^{44}\text{erg s}^{-1}} + \log(1 + \sin i) - 0.5 \log \cos i\ [\text{lt. days}] \quad (4)$$

Table 4. Global parameters of CTS C30.10 from Observation 2.

Mg II line shape	BH mass Kong	L_{bol}/L_{Edd} Kong	BH mass Wang	L_{bol}/L_{Edd} Wang	BH mass Trakhtenbrot	L_{bol}/L_{Edd} Trakhtenbrot
Component 1 only	$6.8 \times 10^8\ M_\odot$	1.6	$1.0 \times 10^9\ M_\odot$	1.1	$1.4 \times 10^9\ M_\odot$	0.8
Component 2 only	$9.9 \times 10^8\ M_\odot$	1.1	$1.4 \times 10^9\ M_\odot$	0.8	$2.0 \times 10^9\ M_\odot$	0.5
Single component fit	$2.4 \times 10^9\ M_\odot$	0.6	$2.7 \times 10^9\ M_\odot$	0.4	$4.9 \times 10^9\ M_\odot$	0.2
Absorption model	$8.5 \times 10^8\ M_\odot$	1.3	$1.2 \times 10^9\ M_\odot$	0.9	$1.7 \times 10^9\ M_\odot$	0.6

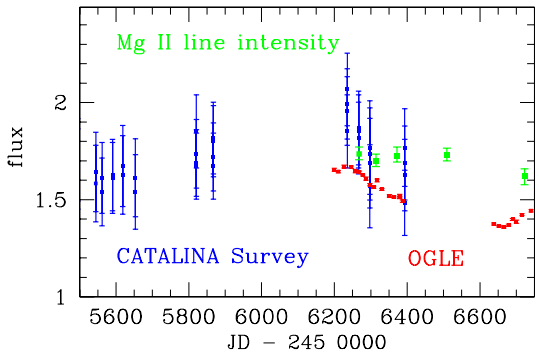

Fig. 7. Time evolution of the V-band flux and the Mg II line intensity. The continuum is in units of 3.77×10^{-16} erg s^{-1} cm^{-2}, and the line flux was scaled by a factor of 1.7×10^{-14} erg s^{-1} cm^{-2}.

give 530 days and 395 days correspondingly, in the rest frame. In this last case, we assumed an inclination angle i of the disk equal to 40 deg and a dust temperature of 1000 K in the Czerny & Hryniewicz (2011) formulae. Thus much longer monitoring is clearly needed.

5. Discussion

We analyzed five long-slit spectroscopic observations of the quasar CTS C30.10 in detail with the aim of determining the shape and the variability of the Mg II broad emission line and the Fe II pseudo-continuum. The object is representative of quasars showing a complex, two-component shape of Mg II, and thus differ qualitatively from single-component quasars like LBQS 2113-4538 (Hryniewicz et al. 2014). According to the Sulentic et al. (2007) classification, CTS C30.10 thus belongs to type B quasars.

5.1. Line properties and quasar variability

Our spectroscopy covers 15 months, and during this period, the source systematically gets fainter, according to OGLE photometry. The source changes the luminosity by 0.23 mag; i.e., it is more variable than the type A quasar studied by us before (amplitude of 0.05 mag in 6 months). This is consistent with spectral classification as a type B source, since in the optical/UV band, the luminosity decreases with the Eddington ratio (e.g., Zuo et al. 2012; Ai et al. 2013).

Our SALT spectroscopic data show that all spectral components do vary. The continuum gets bluer with the decrease in the source luminosity. However, this trend may be an artifact of the behavior of the Balmer continuum, which was not modeled as a separate component. It is known that the Balmer continuum in general strongly contributes to the continuum variability at 3000 Å (e.g., Kokubo et al. 2014). The total EW of the Mg II line systematically rises. This rise is mostly caused by the change in the continuum. The total line luminosity remains constant during the first four observations. At the mean level of $(2.93 \pm 0.03) \times 10^{-14}$ erg s^{-1} cm^{-2}, it drops significantly down to $(2.76 \pm 0.07) \times 10^{-14}$ erg s^{-1} cm^{-2} in the last observation. Thus the change in the line luminosity – only by ∼6% – is much lower than the change in the continuum (∼24%). This is roughly consistent with the Mg II variability level of Mg II line, that is, five times lower than the variability of the continuum found by Kokubo et al. (2014) in SDSS data. The source thus seems to be a typical type B quasar, so well chosen for the monitoring studies.

The total EW of the Mg II line does not depend strongly on whether it is modeled as a single kinematic component or as two separate components. However, the two-component fit is always better than a single-component fit. The second (red) kinematic component is only slightly broader than the first (blue) component, and the relative shift is the same in all five data sets (∼2780 km s^{-1}). Only the first kinematic component of Mg II line has the underlying Fe II contribution. We do not detect any contribution from the NLR with an upper limit of 2%. We also do not detect any significant difference yet between the variability of the two components. Both the direct fitting and the rms study do not point toward different time behavior of the two kinematic components of the Mg II line.

The EW of the Fe II pseudo-continuum measured in the 2700–2900 Å band changes monotonically, but the line intensity is also not monotonic, as for Mg II. The accuracy of its measurement is lower than the Mg II measurement owing to the coupling with the slope of the continuum in data fitting. We do not have a reliable broad band spectrum to measure the continuum slope in the wavelength bands that is relatively free of the Fe II contamination.

Out of the several templates used, the template d12-m20-20-5 of Bruhweiler & Verner (2008), convolved with a Gaussian of dispersion 900 km s^{-1} (Model M in Table 1), is overall the best, but several other theoretical templates are not much worse. This template assumes an order of magnitude higher density 10^{12} cm^{-3} than the best template for type A objects like LBQS 2113-4538 and I Zw 1 (Hryniewicz et al. 2014; Bruhweiler & Verver 2008), with the two other parameters (turbulent velocity and ionization flux) being the same.

5.2. Black hole mass and the broad band spectrum

The two-component character of the Mg II line creates a problem for determining the black hole mass. Our lack of a complete picture of the BLR dynamics leads to a need for some arbitrary choice of whether to use the whole line profile and its FWHM or one of the kinematic components. We fit the broad band spectra for various choices of the formulae and components (see Table 4). Overall, the mass determination based on Component 1 is in reasonable agreement with fitting the Novikov-Thorne model to the broad band spectra ($1.4 \times 10^9\ M_\odot$ for a non-rotating black hole), but the bolometric luminosity seems to be considerably overpredicted by the standard formulae. Disk fitting indicates a lower inclination and a lower Eddington ratio

(only 0.35, more consistently with type B source). The disk fits are not unique, and the black hole mass up to $2.0 \times 10^9\ M_\odot$ is equally good but requires a higher Eddington ratio (up to 0.5) and higher inclination (60 deg). Lower inclination might also explain why the FWHM of Component 1 is relatively low, only ~2800 km s^{-1}. The overall width is much larger, owing to the presence of the second kinematic component. If we allow for a large spin of the black hole, then the black hole mass value based on a single component fit is far more appropriate, and the Eddington ratio in such a fit is much lower. This might favor using the whole line profile. On the other hand, modeling the quasar spectra in the far UV is problematic in most of quasars (see, e.g., Lawrence 2012; but see Czerny et al. 2011 for an example of the successful spin determination based on broad band fitting of SDSS J094533.99+100950.1). Most of the objects show a turn-off at ~1000 Å in the rest frame, corresponding to the maximum of the disk temperature of about 50 000 K (Laor & Davis 2014), and this might result from the vigorous line-driven wind outflow from the disk surface at higher temperatures.

5.3. Two-component BLR region for LIL

Type A quasars show a single component Mg II line of a Lorentzian shape (e.g., Laor et al. 1997b; Veron-Cetty et al. 2001; Sulentic et al. 2002; Zamfir et al. 2010; Sulentic et al. 2009, 2011; Shapovalova et al. 2012), but in type B sources, having a lower Eddington ratio, a second kinematic component appears. Its presence remains unexplained. It might imply that there is another emitting region, or some further reprocessing (absorption or scattering) in the circumnuclear region. It might also be the direct signature of the emission coming from an accretion disk that is expected to have double-peak profile.

The high ionization lines (HIL) show the assymetry and systematic shifts with respect to the NLR, which is naturally interpreted as the result of emission from an outflowing wind. The LILs usually do not show such a strong shift, but the asymmetry clearly appears in some sources, like the one studied here, and a need for a multicomponent fit appears. This is frequently seen in the Hβ structure (e.g., Hu et al. 2012) since this line has been far better studied than Mg II, but the overall trend is similar in both lines (e.g., Marziani et al. 2013b). In the case of our source, we cannot determine the quasar rest frame. We searched for weak narrow emission lines in the available spectrum, but we were unable to identify any of them in a reliable way.

It is interesting to note that radio-loud sources also can display line profiles of the type B. In particular, the Mg II shape of 3C 279 also shows a second, redshifted component, with the velocity shift between the two being on the order of 4000 km s^{-1} (Punsly 2013). Since 3C 279 is a blazar observed at very low inclination angle (below ~5 deg; e.g., Bloom et al. 2013), Punsly (2013) suggests that the red part of Mg II comes from upscattering by the plasma that is either infalling close to the jet axis on the observer's side or outflowing on the counter-jet side. The two components in 3C 279 varied in a different way so both possibilities are equally likely. However, in our case the two components seem to vary in the same way; i.e., the inflow interpretation offers the most probable interpretation. Such a quasi-radial inflow close to the symmetry axis is predicted by the simulations of accretion onto black hole when the accreting material has a range of angular momentum (e.g., Proga & Begelmann 2003). The inflow velocity is close to the local escape velocity, so if the region is radially somewhat more distant than the production region of Mg II, the requested redshift-inducing speed of 2780 km s^{-1} can be achieved. However, in this case the angular extension of the accreting region is large, about 30 deg around the symmetry axis, so the significant velocity gradient would be expected along the line of sight to the observer. On the other hand, jet formation is accompanied by the cocoon developments, and for some parameters the backflowing plasma forms a relatively narrow elongated structure along the jet (e.g., Massaglia et al. 1996). This structure might be a more attractive candidate for the scattering inflowing medium, but in this case the scattering probability becomes too low for obvious geometrical reasons.

On the other hand, long monitoring of the Hβ line shape of NGC 5548 and 3C 390.3 (which belong to B class) shows that the two components actually come from a disk, the relative strength of the two slowly varies with time over the years, and the changes are modeled well by some kind of spiral structure within an accretion disk (see Shapovalova et al. 2009, and the references therein). The separation between the two peaks in NGC 5548 is about 3000 km s^{-1}, so quite similar to what is observed in our source. In other objects, like NGC 4151, the situation is more complex, and a multicomponent origin of Hβ is called for.

5.4. Cosmological application of type B objects at intermediate redshifts

Reverberation studies of quasars can be used as new cosmological probes of the expansion of the Universe (Watson et al. 2011; Czerny et al. 2013; but see also Marziani & Sulentic 2014a; La Franca et al. 2014; Wang et al. 2013 for a different approach). Optical observations of intermediate redshift quasars give an opportunity to observe the Mg II line. Selecting type A objects is an advantage since the shape of the Mg II line is very simple in this class, and the whole line is represented well with a single Lorentzian shape. The line symmetry supports the conclusion about the absence of an inflow and outflow so the motion of the emitting clouds is then likely to be consistent with the Keplerian motion. Type B objects have more complex Mg II lines, so it is not a priori clear whether the reactions of the line components are the same. On the other hand, the overall variability level of type B objects in the optical/UV band is higher (e.g., Papadakis et al. 2000; Klimek et al. 2004, Ai et al. 2013) which makes it easier to determine the time delay. However, the observed variability level of Mg II in CTS C30.10 is still much lower than the continuum variability which is consistent with the reprocessing scenario. In this case we can expect that the line luminosity indeed may reflect the changes in the continuum and the measurement of the delay is likely to be possible. In the case of the CIV monitoring done with HET telescope, the CIV line varied more (Kaspi et al. 2007), and the dominance of the intrinsic changes made the determination of the delay difficult, despite seven years of monitoring.

The underlying Fe II pseudo-continuum complicates the analysis in both types of objects, but it seems that a good theoretical template exists (one of the templates from Bruhweiler & Verner 2008) that can be used almost universally to model this contribution. The quality of the SALT spectroscopy is high enough to measure the EW of the Mg II with an accuracy of ~0.25 Å, despite the Fe II uncertainty.

Acknowledgements. Part of this work was supported by Polish grants Nr. 719/N-SALT/2010/0, UMO-2012/07/B/ST9/04425. The spectroscopic observations reported in this paper were obtained with the Southern African Large Telescope (SALT), proposals 2012-2-POL-003 and 2013-1-POL-RSA-002. J.M., K.H., B.C., M.K., and A.Ś. acknowledge the support by the Foundation for Polish Science through the Master/Mistrz program 3/2012. K.H. also thanks the Scientific Exchange Programme (Sciex) NMSch for the opportunity of working at ISDC. The financial assistance of the South African National Research Foundation (NRF) towards this research is hereby acknowledged (M.B.). The OGLE project has received funding from the European Research Council

under the European Community's Seventh Framework Programme (FP7/2007-2013)/ERC grant agreement no. 246678 to AU. The Fe II theoretical templates described in Bruhweiler & Verner (2008) were downloaded from the web page http://iacs.cua.edu/personnel/personal-verner-feii.cfm with the permission of the authors. Part of this work is based on archival data, software or on-line services provided by the ASI Science Data Center (ASDC). This research has made use of the USNOFS Image and Catalogue Archive operated by the United States Naval Observatory, Flagstaff Station (http://www.nofs.navy.mil/data/fchpix/). This publication makes use of data products from the Wide-field Infrared Survey Explorer, which is a joint project of the University of California, Los Angeles, and the Jet Propulsion Laboratory/California Institute of Technology, funded by the National Aeronautics and Space Administration. This publication makes use of data products from the Two Micron All Sky Survey, which is a joint project of the University of Massachusetts and the Infrared Processing and Analysis Center/California Institute of Technology, funded by the National Aeronautics and Space Administration and the National Science Foundation. The CSS survey is funded by the National Aeronautics and Space Administration under Grant No. NNG05GF22G issued through the Science Mission Directorate Near-Earth Objects Observations Program. The CRTS survey is supported by the U. S. National Science Foundation under grants AST-0909182. Based on observations made with the NASA Galaxy Evolution Explorer. GALEX is operated for NASA by the California Institute of Technology under NASA contract NAS5-98034. This research has made use of the NASA/IPAC Extragalactic Database (NED) which is operated by the Jet Propulsion Laboratory, California Institute of Technology, under contract with the National Aeronautics and Space Administration.

References

Ai, Y. L., Yuan, W., Zhou, H., et al. 2013, AJ, 145, 90
Bentz, M. C., Denney, K. D., Grier, C. J., et al. 2013, ApJ, 767, 149
Betoule, M., Kessler, R., Guy, J., et al. 2014, A&A, 568, A22
Bloom, S. D., Fromm, C. M., & Ros, E. 2013, AJ, 145, 12
Bordoloi, R., Lilly, S. J., Kacprzak, G. G., & Churchill, C. W. 2014, ApJ, 784, 108
Bruhweiler, F., & Verner, E. 2008, ApJ, 675, 83
Burgh, E. B., Nordsieck, K. H., Kobulnicky, H. A., et al. 2003, SPIE, 4841, 1463
Cardelli, J. A., Clayton, G. C., & Mathis, J. S. 1989, ApJ, 345, 245
Clavel, J., Reichert, G. A., Alloin, D., et al. 1991, ApJ, 366, 64
Collin-Souffrin, S., Dyson, J. E., McDowell, J. C., & Perry, J. J. 1988, MNRAS, 232, 539
Crawford, S. M., Still, M., Schellart, P., et al. 2010, PySALT: the SALT Science Pipeline, SPIE Astronomical Instrumentation, 7737, 25
Czerny, B., & Hryniewicz, K. 2011, A&A, 525, L8
Czerny, B., Hryniewicz, K., Nikołajuk, M., & Sądowski, A. 2011, MNRAS, 415, 2942
Czerny, B., Hryniewicz, K., Maity, I., et al. 2013, A&A, 556, A97
Dietrich, M., Hamann, F., Shields, J. C., et al. 2002, ApJ, 581, 912
Dietrich, M., Hamann, F., Appenzeller, I., & Vestergaard, M. 2003, ApJ, 596, 817
Drake, A. J., Djorgovski, S. G., Mahabal, A., et al. 2009, ApJ, 696, 870
Elvis, M., Hao, H., Civano, F., et al. 2012, ApJ, 759, 6
Ferland, G., Hu, C., Wang, J.-M., et al. 2009, ApJ, 707, L82
Ferland, G. J., Porter R. L., van Hoof P. A. M., et al. 2013, Rev. Mex. Astron. Astrofis., 49, 137
Goad, M. R., Koratkar, A. P., Axon, D. J., Korista, K. T., & O'Brien, P. T. 1999, ApJ, 512, L95
Hoenig, S. F. 2014, ApJ, 784, L4
Hryniewicz, K., Czerny, B., Pych, W., et al. 2014, A&A, 562, A34
Hu, C., Wang, J.-M., Ho, L. C., et al. 2008, ApJ, 687, 78
Hu, C., Wang, J.-M., Ho, L. C., et al. 2012, ApJ, 760, 126
Kaspi, S., Smith, P. S., Netzer, H., et al. 2000, ApJ, 533, 631
Kaspi, S., Brandt, W. N., Maoz, D., et al. 2007, ApJ, 659, 997
Kelly, B. C., Vestergaard, M., Fan, X., et al. 2010, ApJ, 719, 1315
Klimek, E. S., Gaskell, C. M., & Hedrick, C. H. 2004, ApJ, 609, 69
Kobulnicky, H. A., Willmer, C. N. A., Phillips, A. C., et al. 2003, ApJ, 599, 1006
Kokubo, M., Morokuma, T., Minezaki, T., et al. 2014, ApJ, 783, 46
Kong, M.-Z., Wu, X.-B., Wang, R., & Han, J.-L. 2006, Chin. J. Astron. Astrophys., 6, 396
Korista, K. T., & Goad, M. R. 2004, ApJ, 606, 749
La Franca, F., Bianchi, S., Ponti, G., Branchini, E., & Matt, G. 2014, ApJ, 787, L12
Laor, A., & Davis, S. 2014, MNRAS, 438, 3024
Laor, A., Fiore, F., Elvis, M., Wilkes, B. J., & McDowell, J. C. 1997a, ApJ, 477, 93
Laor, A., Jannuzi, B. T., Green, R. F., & Boroson, T. A. 1997b, ApJ, 489, 656
Lawrence, A. 2012, MNRAS, 423, 451
MacAlpine, G. M. 2003, Rev. Mex. Astron. Astrofis., 18, 63
Martin, D. C., Fanson, J., Schiminovich, Da., et al. 2005, ApJ, 619, L1
Marziani, P., & Sulentic, J. W. 2014a, Adv. Space Res., 54, 1331
Marziani, P., & Sulentic, J. W. 2014b, MNRAS, 442, 1211
Marziani, P., Sulentic, J. W., Stirpe, G. M., Zamfir, S., & Calvani, M. 2009, A&Ap, 495, 83
Marziani, P., Sulentic, J. W., Plauchu-Frayn, I., & del Olmo, A. 2013a, ApJ, 764, 150
Marziani, P., Sulentic, J. W., Plauchu-Frayn, I., & del Olmo, A. 2013b, A&A 555, A89
Massaglia, S., Bodo, G., & Ferrari A. 1996. A&A, 307, 997
Maza, J., Ruiz, M. T., Gonzalez, L. E., Wischnjewsky, M., &Antezana, R. 1993, Rev. Mex. Astron. Astrofis., 25, 51
Metzroth, K. G., Onken, C. A., Peterson, B. M., et al. 2006, ApJ, 647, 901
Morton, D. C. 1991, ApJS, 77, 119
Papadakis, I. E., Brinkmann, W., Negoro, H., et al. 2000 [arXiv:astro-ph/0012317]
Peterson, B. M. 1993, PASP, 105, 247
Peterson, B. M., Ferrarese, L., Gilbert, K. M., et al. 2004, ApJ, 613, 682
Proga, D., & Begelman, M. C. 2003, ApJ, 582, 69
Punsly, B. 2013, ApJ, 762, L25
Reichert, G. A., Rodriguez-Pascual, P. M., Alloin, D., et al. 1994, ApJ, 425, 582
Richards, G. T. 2006, AJ, 131, 2766
Rozanska, A., Nikolajuk, M., Czerny, B., et al. 2014, New Astron., 28, 7
Sargent, W. L. W. 1977, in Evolution of Galaxies and Stellar Populations, Proc. of a Conference at Yale University, May 19–21, eds. M. T. Beatrice, & B. L. Richard (New Haven: Yale University Observatory), 427
Schlafly, E. F., & Finkbeiner, D. P. 2011, ApJ, 737, 103
Shapovalova, A. I., Popovic, L. C., Bochkarev, N. G., et al. 2009, New Astron. Rev., 53, 191
Shapovalova, A. I., Popovic, L. C., Burenkov, A. N., et al. 2012, ApJS, 202, 10
Shen, Y., & Liu, X. 2012, ApJ, 753, 125
Shen, Y., Greene, J. E., Strauss, M. A., Richards, G. T., & Schneider, D. P. 2008, ApJ, 680, 169
Shen, Y., Richards, G. T., Strauss, M. A., et al. 2011, ApJS, 194, 45
Skrutskie M. F., Cutri, R. M., Stiening, R., et al. 2006, AJ, 131, 1163
Smith, M. P., Nordsieck, K. H., Burgh, E. B., et al. 2006, in SPIE Conf. Ser., 6269
Sulentic, J. W., Marziani, P., Zamanov, R., et al. 2002, ApJ, 566, L71
Sulentic, J. W., Bachev, R., Marziani, P., Negrete, C. A., & Doltzin, D. 2007, ApJ, 666, 757
Sulentic, J. W., Marziani, P., & Zamfir, S. 2009, New Astron. Rev., 53, 198
Sulentic, J., Marziani, P., & Zamfir, S. 2011, Balt. Astron., 20, 427
Trakhtenbrot, B., & Netzer, H. 2012, MNRAS, 427, 3081
Tsuzuki, Y., Kawara, K., Yoshi, Y., et al. 2006, ApJ, 650, 5
Vanden Berk, D. E., Richards, G. T., Bauer, A., et al. 2001, AJ, 122, 549
Veron-Cetty, M.-P., Veron, P., & Goncalves, A. C. 2001, A&A, 372, 730
Vestergaard, M., & Osmer, P. S. 2009, ApJ, 699, 800
Vestergaard, M., & Wilkes, B. 2001, 134, 1
Voges W., Richards, G. T., Bauer, A., et al. 1999, A&A, 349, 389
Udalski, A. 2003, Acta Astron. 53, 291
Wandel, A., Peterson, B. M., & Malkan, M. A. 1999, ApJ, 526, 579
Wang, J.-G., Dong, X.-B., Wang, T.-G., et al. 2009, ApJ, 707, 1334
Wang, J.-M., Du, P., Valls-Gabaud, D., Hu, C., & Netzer, H. 2013, Phys. Rev. Lett., 110, 081301
Watson, D., Denney, K. D., Vestergaard, M., & Davis, T. M. 2011, ApJ, 740, L49
Woo, J.-H. 2008, AJ, 135, 1849
Wright, E. L., Eisenhardt, P. R. M., Mainzer, A. K., et al. 2010, AJ, 140, 1868
Yoshii, Y., Kobayashi, Y., Minezaki, T., Koshida, S., & Peterson, B. A. 2014, ApJ, 784, L11
Zamfir, S., Sulentic, J. W., Marziani, P., & Dulcin, D. 2010, MNRAS, 403, 1759
Zuo, W., Wu, X.-B., Liu, Y.-Q., & Jiao, C.-L. 2012, ApJ, 758, 104

Pages 12 to 13 are available in the electronic edition of the journal at http://www.aanda.org

Table 1. Parameters of the fits for the five individual spectra obtained with SALT between December 2012 and March 2014.

Model	Shape[a]	Fe II template	Slope	Mg II *EW* Å	Mg II *EW* comp. 1 Å	Mg II *FWHM* comp. 1 km s^{-1}	Mg II *EW* comp. 2 Å	Mg II *FWHM* comp. 2 km s^{-1}	Fe II *EW* Å	χ^2
Obs. 1										
A	DL	temp 01	–1.4	35.08	14.4	3243	20.7	7479	8.35	300.47
B	DL	temp 02	–1.6	29.52	12.9	2812	16.6	6870	6.36	273.62
C	DL	temp 03	–1.3	25.00	16.8	2775	8.2	3145	8.95	233.64
D	DL	temp 04	–1.3	25.27	17.0	2825	8.3	3239	8.69	232.89
E	DL	temp 05	–1.3	24.89	17.0	2846	7.9	3142	7.84	236.32
F	DL	temp 06	–1.2	25.33	17.1	2912	8.2	3351	7.86	234.16
G	DL	temp 07	–1.2	24.90	16.9	2918	8.0	3408	5.56	237.73
H	DL	temp 08	–1.2	25.09	17.0	2934	8.1	3420	6.36	237.20
I	DL	temp 09	–1.2	25.23	17.0	2850	8.2	3251	8.79	232.58
J	DL	temp 10	–1.2	25.56	17.3	2912	8.3	3345	8.80	232.45
K	DL	temp 11	–1.1	25.97	17.6	2931	8.4	3298	10.54	229.89
L	DL	temp 12	–1.2	25.47	17.1	2909	8.3	3433	7.27	233.22
M	DL	temp 13	–1.2	25.63	17.1	2871	8.5	3470	6.98	230.78
N	SL	temp 13	–0.7	26.37	–	5022	–	–	2.31E-04	1155.71
O	DG	temp 13	–0.9	37.89	25.50	17344	12.4	4259	0.35	687.22
P	SG	temp 13	–0.6	18.37	- -	5515	–	–	4.92E-02	1593.88
Q	DL	temp 14	–1.2	25.52	16.9	2878	8.7	3520	7.40	230.13
R	DL	temp 15	–1.2	25.30	17.4	2950	8.0	3251	8.26	234.82
S	DL	temp 16	–1.4	24.83	16.8	2962	8.1	3604	3.79	281.96
Obs. 2										
A	DL	temp 01	–1.1	28.96	23.4	3725	5.6	2991	6.11	447.57
B	DL	temp 02	–1.1	25.73	17.5	2990	8.2	3606	9.34	430.38
C	DL	temp 03	–1.2	25.75	16.6	2771	9.1	3144	9.77	426.84
D	DL	temp 04	–1.2	25.99	16.8	2825	9.2	3225	9.45	435.04
E	DL	temp 05	–1.2	25.61	16.9	2868	8.7	3172	8.16	440.35
F	DL	temp 06	–1.1	26.09	17.1	2931	9.0	3334	8.59	433.52
G	DL	temp 07	–1.1	25.44	16.8	2940	8.7	3369	5.72	431.87
H	DL	temp 08	–1.1	25.76	17.0	2962	8.9	3409	6.72	438.81
I	DL	temp 09	–1.1	26.04	17.0	2828	9.2	3181	10.53	421.85
J	DL	temp 10	–1.1	26.39	17.2	2925	9.2	3316	9.93	431.14
K	DL	temp 11	–1.0	26.93	17.6	2937	9.3	3238	12.36	424.05
L	DL	temp 12	–1.1	26.24	17.0	2928	9.2	3422	7.92	434.13
M	DL	temp 13	–1.1	26.51	16.9	2850	9.6	3438	8.38	422.49
N	SL	temp 13	–0.5	28.18	–	5316	–	–	2.30E-04	1017.32
O	DG	temp 13	–0.8	20.85	14.1	3326	6.7	3274	12.78	469.17
P	SG	temp 13	–0.5	19.31	–	5703	–	–	2.82E-04	1247.38
Q	DL	temp 14	–1.1	25.85	16.9	2956	9.0	3450	6.38	430.29
R	DL	temp 15	–1.1	26.13	17.4	2978	8.7	3238	9.12	435.09
S	DL	temp 16	–1.3	25.42	16.2	2865	9.2	3461	5.87	446.53
Obs. 3										
A	DL	temp 01	–1.2	29.47	25.4	3565	4.1	2098	5.65	234.74
B	DL	temp 02	–1.1	26.78	21.0	2862	5.8	2498	13.63	208.81
C	DL	temp 03	–1.3	26.54	19.4	2718	7.2	2401	10.36	202.99
D	DL	temp 04	–1.3	26.97	19.6	2725	7.4	2433	11.47	204.55
E	DL	temp 05	–1.3	26.70	19.6	2721	7.2	2339	11.36	207.27
F	DL	temp 06	–1.1	27.06	19.8	2811	7.3	2484	11.14	204.57
G	DL	temp 07	–1.1	26.19	19.4	2846	6.8	2529	6.92	207.22
H	DL	temp 08	–1.1	26.51	19.6	2865	6.9	2536	8.13	207.98
I	DL	temp 09	–1.1	26.87	19.6	2750	7.3	2423	11.80	200.30
J	DL	temp 10	–1.1	27.57	20.0	2790	7.6	2470	13.49	203.87
K	DL	temp 11	–1.0	28.29	20.6	2812	7.7	2417	16.40	200.53
L	DL	temp 12	–1.1	26.83	19.8	2859	7.1	2561	8.47	206.03
M	DL	temp 13	–1.1	27.45	19.7	2750	7.8	2636	10.21	202.69
N	SL	temp 13	–0.7	28.91	–	4900	–	–	2.64E-04	494.53
O	DG	temp 13	–1.0	47.39	34.2	18130	13.2	4039	0.88	371.37
P	SG	temp 13	–0.6	20.35	–	5412	–	–	0.79	654.71

Notes. Templates are numbered in the following way: temp 1 is the observational template from Vestergaard & Wilkes (2001), temp 2 is the observational template of Tsuzuki et al. (2006), templates 3–15 are theoretical templates of Bruhweiler & Verner (2008), designated as d11-m20-20.5-735, d11-m30-20-5-735, d11-m20-21-735, d10-5-m20-20-5, d11-m05-20-5, d11-m10-20-5, d11-m20-20-5, d11m30-20-5, d11-m50-20-5, d11-5-m20-20-5, d12-m20-20-5, d11-m20-20,d11-m20-21 in their paper, and template 16 is the observational template from Hryniewicz et al. (2014). [(a)] Line shape: single/double Gaussian or Lorentzian.

Table 1. continued.

Model	Shape[a]	Fe II template	Slope	Mg II *EW* Å	Mg II *EW* comp. 1 Å	Mg II *FWHM* comp. 1 km s^{-1}	Mg II *EW* comp. 2 Å	Mg II *FWHM* comp. 2 km s^{-1}	Fe II *EW* Å	χ^2
Q	DL	temp 14	–1.2	26.86	19.5	2825	7.3	2636	8.77	204.81
R	DL	temp 15	–1.1	27.26	20.1	2834	7.1	2383	12.69	205.16
S	DL	temp 16	–1.3	26.12	18.9	2756	7.2	2595	7.25	223.20
Obs. 4										
A	DL	temp 01	–1.8	41.92	10.6	2815	31.4	7509	10.02	683.98
B	DL	temp 02	–1.5	29.38	19.7	2806	9.7	3578	25.02	601.94
C	DL	temp 03	–1.8	28.47	17.8	2698	10.7	3209	14.63	609.77
D	DL	temp 04	–1.8	28.77	18.1	2791	10.7	3350	13.49	611.58
E	DL	temp 05	–1.8	28.44	18.1	2787	10.3	3206	13.62	620.40
F	DL	temp 06	–1.6	29.03	18.4	2921	10.7	3525	12.61	612.65
G	DL	temp 07	–1.6	28.32	17.9	2903	10.4	3594	9.43	617.59
H	DL	temp 08	–1.6	28.65	18.2	2953	10.5	3619	10.37	620.76
I	DL	temp 09	–1.6	28.83	18.2	2831	10.6	3378	14.01	605.40
J	DL	temp 10	–1.5	29.60	18.5	2887	11.1	3488	15.32	609.19
K	DL	temp 11	–1.5	30.36	19.0	2921	11.4	3413	18.35	605.11
L	DL	temp 12	–1.6	29.21	18.3	2915	10.9	3631	11.58	612.29
M	DL	temp 13	–1.6	29.47	18.3	2850	11.2	3666	11.30	604.04
N	SL	temp 13	–1.0	31.44	–	5644	–	–	2.24E-04	1738.84
O	DG	temp 13	–1.3	23.38	15.4	3288	7.9	3389	17.98	682.53
P	SG	temp 13	–0.9	22.05	–	6213	–	–	0.00	2205.63
Q	DL	temp 14	–1.6	29.33	17.8	2846	11.5	3716	12.34	605.93
R	DL	temp 15	–1.5	29.17	18.8	2943	10.4	3347	14.62	615.34
S	DL	temp 16	–1.8	28.27	17.2	2881	11.1	3839	7.91	711.19
Obs. 5										
A	DL	temp 01	–1.9	42.63	8.1	2193	34.5	6988	10.30	307.59
B	DL	temp 02	–1.6	29.53	20.6	2750	8.9	3363	20.66	241.24
C	DL	temp 03	–1.9	28.97	19.0	2639	10.0	3022	13.38	243.12
D	DL	temp 04	–1.9	29.25	19.2	2698	10.1	3116	12.82	241.99
E	DL	temp 05	–1.8	28.81	19.2	2709	9.6	2997	12.25	248.03
F	DL	temp 06	–1.6	29.33	19.4	2796	9.9	3197	12.13	235.25
G	DL	temp 07	–1.7	28.66	18.9	2765	9.7	3241	9.45	235.95
H	DL	temp 08	–1.7	28.89	19.2	2821	9.7	3253	9.96	237.44
I	DL	temp 09	–1.6	29.25	19.2	2705	10.0	3084	13.94	234.95
J	DL	temp 10	–1.6	29.72	19.6	2781	10.2	3181	13.96	235.08
K	DL	temp 11	–1.6	30.47	20.2	2812	10.3	3142	16.67	235.54
L	DL	temp 12	–1.7	29.52	19.4	2778	10.1	3261	11.63	235.43
M	DL	temp 13	–1.7	29.82	19.3	2728	10.5	3338	11.21	232.07
N	SL	temp 13	–1.1	30.69	–	5122	–	–	2.85E-04	1134.71
O	DG	temp 13	–1.4	23.93	16.18	3142	7.8	3106	18.22	268.18
P	SG	temp 13	–1.0	21.51	–	5713	–	–	2.41E-09	1555.81
Q	DL	temp 14	–1.7	29.66	19.0	2715	10.8	3366	12.41	231.64
R	DL	temp 15	–1.6	29.41	19.8	2831	9.6	3075	13.35	238.80
S	DL	temp 16	–1.9	28.29	18.5	2800	9.8	3426	6.64	313.02